



Processing of NaCl powders of controlled size and shape for the microstructural tailoring of aluminium foams

C. Gaillard^a, J.F. Despois^b, A. Mortensen^{b,*}

^a Centre Interdisciplinaire de Microscopie Electronique, Swiss Federal Institute of Technology (Ecole Polytechnique Fédérale de Lausanne-EPFL), CH-1015 Lausanne, Switzerland

^b Laboratory for Mechanical Metallurgy, Swiss Federal Institute of Technology (Ecole Polytechnique Fédérale de Lausanne-EPFL), CH-1015 Lausanne, Switzerland

Received 23 October 2003; received in revised form 20 February 2004

Abstract

NaCl powders are prepared by anti-solvent crystallisation, varying in controlled fashion the morphology and size of resulting powders. These powders are then used to produce open-cell pure aluminium foams by infiltration, using the replication process. The microstructure and the compressive mechanical behaviour of these foams are compared with those of similar foams made using commercial NaCl powders of less regular shape and size. It is found that, while the foam pore shape does not influence strongly the initial power-law behaviour of the foam, it causes variations in the strain at which the foam deviates from power-law behaviour.

© 2004 Published by Elsevier B.V.

Keywords: Sodium chloride; Crystallisation; Infiltration; Replication process; Aluminium foam; Compressive behaviour

1. Introduction

There exists at present a relatively wide palette of methods for the production of metal foams; these are comprehensively reviewed in several recent publications [1,2]. Amongst current foam-production methods, the replication technique is well suited for the production of uniform and fine open-cell foams of lower melting-point metals such as aluminium [3]. Replication processing consists in infiltrating a leachable porous preform of sintered powder that is subsequently removed by dissolution. Given its low cost, its chemical inertness in contact with aluminium, its relatively high melting point and its ease of dissolution in water, sodium chloride (NaCl) is often used as the preform filler material for aluminium foams [4–6].

In replicated foams, the pore shape is predominantly controlled by the initial shape of the leachable powder that was used to produce the infiltrated preform: save for powder geometry changes induced while bonding the preform, pores of the resulting foam “replicate” the initial shape of these

powder particles. Changing the shape of the powder used to produce the preform therefore provides a pathway for the exploration of microstructure/property relations in open-pore metal foams.

As with many water-soluble inorganic salts, industrial production of NaCl crystals is generally conducted by evaporative crystallisation. When NaCl crystallisation is conducted from brine under slow evaporation conditions, large cube-like transparent crystals are obtained. With an aim to reduce energy costs in NaCl production, a new route has recently been developed, named anti-solvent crystallisation. This consists in inducing precipitation of NaCl crystals from brine by adding a second “anti-solvent” liquid, in the presence of which the solubility of NaCl drops significantly. Classical organic anti-solvents include 2-isopropoxyethanol [7], *N*-dimethylisopropylamine [8] or *N*-diisopropylamine [9]. The resulting NaCl particles possess relatively large sizes and feature a bimodal distribution; however, it has been shown that NaCl particles of narrowly distributed size in the range 2–3 μm can be produced using acetone as the anti-solvent [10].

An interesting feature of anti-solvent precipitation is that it affords some level of control over particle size and shape. The main factors influencing crystal growth and morphology with this technique can be classified in two main categories:

* Corresponding author. Tel.: +41-21-693-2912; fax: +41-21-693-4664.

E-mail address: andreas.mortensen@epfl.ch (A. Mortensen).

- 65 (i) chemical parameters including the composition of the
66 solution (presence of additives or impurities), supersaturation level and pH-value and;
67
68 (ii) physical parameters including temperature, stirring and
69 reaction time.

70 Each of these factors can contribute by influencing the
71 thermodynamics of precipitation or via kinetic effects [11].
72 Specifically, additives can affect nucleation, agglomeration
73 and crystal shape by selectively accelerating or slowing the
74 growth of certain crystal facets [12].

75 These facts motivated the present study, in which we explore the production of NaCl particles featuring new morphologies via the precipitation technique, using alcohol and organic additives. We produce replicated aluminium foams using these powders and assess their mechanical behaviour by means of compression testing of miniature specimens, with a goal to explore the influence of pore morphology on the deformation behaviour of open-celled metal foams.

83 2. Experimental procedure

84 2.1. Materials

85 Citric acid (C(OH)(COOH)(CH₂COOH)₂; 99.5 mass%),
86 poly(acrylic acid) (MW 2000), sodium hydroxide and
87 ethanol were all purchased from Aldrich (Buchs, Switzerland). The NaCl powder (99% purity) used to prepare the solutions was purchased from Fluka Chemika (Buchs, Switzerland). Fine NaCl used in the virgin state for preform preparation and infiltration (called hereafter “commercial salt”) was purchased from Salines de Bex SA (Bex, Switzerland) under the denomination “CP1”. Prior to infiltration, the commercial salt was sieved to narrow its particle size distribution.

96 2.2. Preparation of precipitated sodium chloride particles

97 Different NaCl powders were prepared by precipitation
98 using aqueous and organic liquids. Saturated brine was prepared by dissolving 450 g Fluka NaCl powder in one litre of

distilled water. The organic liquid was produced either by
100 dissolving solid organic additive (polyacrylic acid or citric
101 acid) directly in ethanol, or alternatively by mixing 1 mol/l
102 sodium hydroxide solution with ethanol. Precipitation was
103 then carried out in a glass vessel by rapid addition of a
104 controlled volume of brine into the organic solution under
105 ambient conditions. The mixture was homogenised by magnetic
106 stirring at 370 rpm. Depending on the powder lot produced,
107 stirring was maintained (Powders I, IV, VI and VII)
108 or stopped after 30 s (Powders II, III and V). The total precipitation
109 time was varied in one instance, with a goal to observe the
110 influence of powder particle coarsening. The resulting precipitates
111 were then filtered, washed twice with ethanol, and dried under vacuum
112 for about 5 h. Experimental parameters defining the seven powder lots
113 produced in this work are given in Table 1.

116 2.3. Preparation of aluminium foams by the replication process

118 Aluminium foams were prepared using Powders IV, V
119 and VI; these are respectively called Foams IV, V and VI. NaCl preforms
120 were first prepared by cold isostatic pressing (CIPing) the NaCl powder
121 in a silicone rubber mould (of internal diameter 20 mm and internal height
122 20 mm) for 1 min under 12.7 MPa.

124 These NaCl preforms were infiltrated with molten pure
125 (99.99%) aluminium heated to 710 °C under 10 MPa argon gas and then
126 solidified directionally. The Al/NaCl composites so produced were
127 machined to produce metallographic samples and cylindrical compression
128 test specimens. The salt pattern was then finally dissolved by immersion
129 in distilled water.

131 2.4. Microstructural characterisation

132 NaCl crystal X-ray diffractograms were obtained under
133 Cu K radiation using a Siemens Model D500 diffraction apparatus
134 (Munich, Germany). Powder compositions were determined using IR
135 transmittance spectra in the range from 400 to 2000 cm⁻¹ recorded with 256 scans on a Nicolet 510

Table 1
NaCl precipitation parameters

Powder number	Organic solution			Aqueous solution Volume (ml)	Precipitation parameters		
	Ethanol volume (ml)	Additive	Additive concentration (mol/l)		Sustained stirring	Time (min)	Yield of reaction (%)
I	10	Polyacrylic acid	0.06	5	Yes	45	6.8
II	20	Sodium hydroxyde ^a	0.20	5	No	30	21
III	20	Citric acid	1.02	10	No	30	20.3
IV	20	Citric acid	0.06	10	Yes	45	21.1
V	300	Citric acid	1.02	150	No	60	21.4
VI	20	Citric acid	1.02	10	Yes	30	17.1
VII	20	None	–	10	Yes	60	22.3

^a In this case the total volume of the organic solution is equal to 25 ml which corresponds to 5 ml of 1 mol/l sodium hydroxide solution and 20 ml of ethanol.

136 FT-IR spectrometer (Madison, USA). The size and morphol-
 137 ogy of NaCl particles or pores in aluminium foams were
 138 examined by low voltage scanning electron microscopy of
 139 powders directly deposited on an aluminium stub without
 140 gold sputtering, using a Philips SFEG high-resolution scan-
 141 ning electron microscope (Eindhoven, The Netherlands).

142 As particles have a cubic aspect, characteristic dimen-
 143 sions of each particle are quantified using their Féret diam-
 144 eter (largest axis between two parallel tangents on opposite
 145 sides of the particle) and by their aspect ratio (ratio between
 146 the largest axis to the minor one) [13,14]. For all experi-
 147 ments, the mean Féret number and the mean aspect ratio

were calculated by counting approximately 50–80 particles
 on several scanning electron micrographs.

Foams were characterised and examined using standard
 techniques of metallographic preparation and observation,
 using the optical and the scanning electron microscope.

2.5. Mechanical testing of the aluminium foams

Compression tests were performed on a screw-driven
 10 kN universal testing machine. Spherically aligned platens
 were used, after coating their surfaces with Teflon spray so
 as to reduce friction with the specimen end surface. All tests


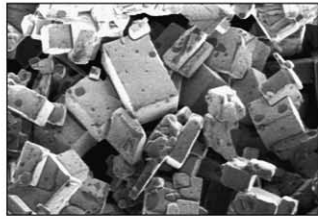

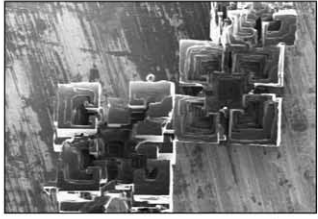

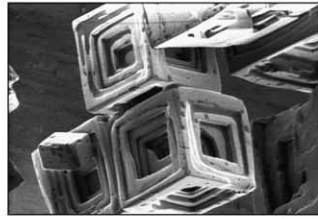
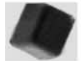
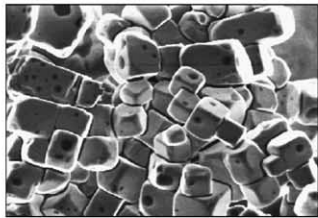
Experiment n°	Morphology	Mean Feret number (standard deviation)	Mean aspect ratio (standard deviation)	S.E.M. micrographs
I (additive: 0.06 M polyacrylic acid)	Polydisperse rectangular particles. 	12.1 μm (5.7 μm)	1.8 (0.5)	 (1.I) 20 μm
II (additive: 0.2 M sodium hydroxyde)	Four-leaf clover-like particles. 	58.2 μm (5.9 μm)	1.1 (0.1)	 (1.II) 50 μm
III (additive: 1 M citric acid)	Pierced cube-like particles. 	46.6 μm (6.7 μm)	1.1 (0.2)	 (1.III) 20 μm
IV (additive: 0.06 M citric acid)	Small cubic particles. 	3.3 μm (1.1 μm)	1.2 (0.2)	 (1.IV) 10 μm

Fig. 1. Influence of chemical parameters on the NaCl crystal morphology. SEM micrographs of NaCl powders precipitated in presence of (1(I)) polyacrylic acid; (1(II)) sodium hydroxide; (1(III)) high citric acid concentration and (1(IV)) lower citric acid concentration.

157 were run in crosshead displacement control at a speed of
158 2 $\mu\text{m/s}$. The deformation of the foam was monitored using
159 three LVDTs with a resolution of 1 μm located symmetrically
160 around the specimen so as to verify that the platens
161 remain parallel during the test.

162 Due to the small amounts of powder produced by precipi-
163 tation, it was only possible to produce and test sub-sized
164 compression specimens; these had a diameter of approxi-
165 mately 15 mm and a height between 2 and 5 mm depending
166 on powder lot size. Cylinders with a diameter of 20 mm and
167 a height of 20 mm were machined from the foam produced
168 with commercial NaCl powder.

169 3. Results

170 3.1. NaCl powder precipitation

171 NaCl powders can be precipitated by pouring an aqueous
172 NaCl solution in ethanol, as this reduces sharply the solu-

173 bility of NaCl [15]. Powder VII, produced in this manner
174 without additives, comprised polydispersed aggregated cu-
175 bic particles. Additives were therefore studied, with a goal
176 to improve the NaCl powder shape and size distribution.

177 Powders I–III were produced in order to test the influ-
178 ence of the additive nature on the NaCl powder morphology.
179 Three different additives were explored: a polymeric addi-
180 tive (polyacrylic acid, Powder I), a basic additive (sodium
181 hydroxide, Powder II) and tricarboxylic acid (citric acid,
182 Powder III). Results are given in Fig. 1.

183 When a polymeric additive is used (Powder I), parallelepipedic
184 powders are obtained, somewhat elongated along one
185 axis with perpendicular flat faces Fig. 1(I). This is reflected
186 in an average aspect ratio equal to 1.8 ± 0.5 for this powder.

187 The two other additives result in equiaxed particles, of
188 aspect ratio around 1.1–1.2 (Fig. 1). Using sodium hydroxide
189 as the additive (Powder II), the NaCl crystal morphology
190 changes to what can be described as four-leafed clover-like
191 cuboidal particles Fig. 1(II). A third morphology is obtained
when citric acid in ethanol is employed as the organic phase,


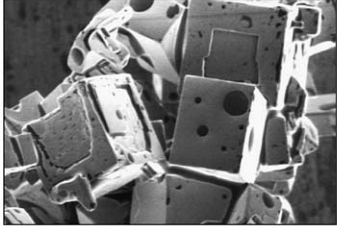
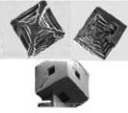
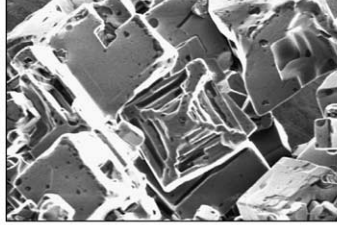
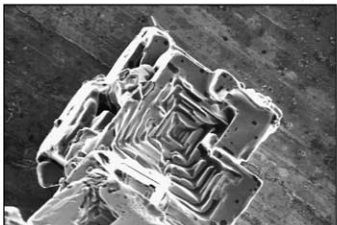
Experiment n°	Morphology	Mean Féret number (standard deviation)	Mean aspect ratio (standard deviation)	S.E.M. micrographs
V (without stirring, longer maturation time)	Large filled cube-like particles. 	44.3 μm (5.1 μm)	1.2 (0.3)	 (2.V) 50 μm
VI (Stirring, shorter maturation time)	Mixture of pierced cube-like particles and of hollow pyramid-like particles: (a) top view - (b) bottom view of smaller fragments. 	24.4 μm (9.9 μm)	1.3 (0.1)	 (2.VI.a) 20 μm  (2.VI.b.) 20 μm

Fig. 2. Influence of physical parameters on the NaCl crystal morphology. SEM micrographs of NaCl powders precipitated in presence of 1 mol/l citric acid with a longer maturation time (2(V)) or magnetic stirring (2(VI) (a) and (b)).

192 Powder III: cubical particles featuring a stepped pyramidal
193 hollow on each facet Fig. 1(III)).

194 The influence of variations in the concentration of
195 citric acid was explored with Powder IV, produced us-
196 ing 0.06 mol/l citric acid (instead of 1 mol/l for Powder
197 III), with stirring maintained throughout precipitation. Far
198 smaller and neatly cubical unagglomerated particles are
199 obtained Fig. 1(IV)). This powder features the most homo-
200 geneous grain size distribution of all, with the lowest size
201 dispersion.

202 The influence of precipitation physical conditions was
203 tested with Powders V and VI. Fig. 2 presents the corre-
204 sponding micrographs. These are to be compared with Pow-
205 der III. Powder V was held for 60 instead of 30 min, allowing
206 more time for particle coarsening. Filled cubical particles of
207 roughly the same size are obtained Fig. 2(V)). Powder VI
208 was stirred, as opposed to Powders III and V, which were
209 not. The major changes induced by stirring are the produc-
210 tion of particle fragments and a mixture of two main mor-
211 phologies: hollow pyramid-faced cubical particles with more
212 closed surfaces than Powder III, and hollow single-pyramid
213 particles. The F eret number distribution is also more scat-
214 tered.

215 Powder infrared spectra were gathered to investigate the
216 presence or absence of the additive on the surface of the par-
217 ticles. The reference spectrum of pure citric acid Fig. 3(a),
218 shows the characteristic stretching vibration bands of car-
219 boxyl groups at about 1730 cm^{-1} , together with other group
220 vibrations causing two characteristic band series in the
221 ranges $1100\text{--}1200$ and $1300\text{--}1400\text{ cm}^{-1}$. The other spectra
222 of Fig. 3 correspond to the powders synthesized with low
223 (0.06 mol/l, Powder IV) or high (1 mol/l, Powders III, V
224 and VI) citric acid concentration. It appears that citric acid
225 is only adsorbed onto the powders prepared with the 1 mol/l

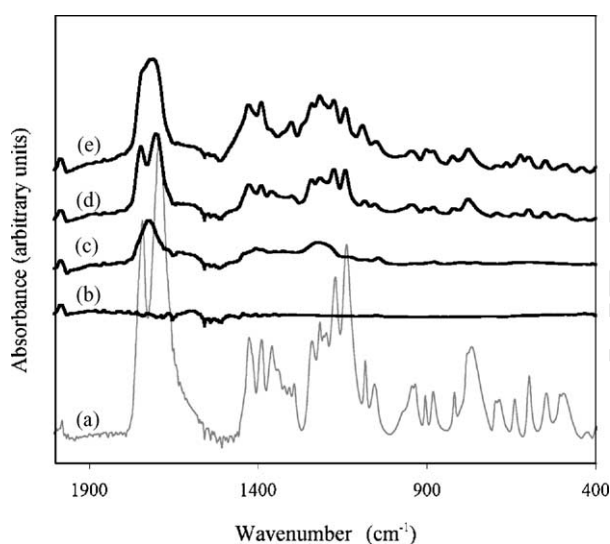


Fig. 3. Infrared spectra of the NaCl powders precipitated in presence of citric acid. (a) Pure citric acid; (b) Powder IV; (c) Powder III; (d) Powder V and (e) Powder VI.

226 solution Fig. 3(c)–(e)). The infrared spectrum of Powder
227 II was also measured, to find that there is no evidence for
228 the adsorption of ethanolate anions since no methyl group
229 vibrations were observed.

230 X-ray diffraction patterns were also gathered on the pow-
231 ders. When comparing these X-ray patterns to those of com-
232 mercial purity NaCl, no detectable difference in peak posi-
233 tion can be found. It thus appears that citric acid does not
234 penetrate into the crystals.

3.2. The metallic foams

235
236 Fig. 4 contains micrographs of the aluminium foams ob-
237 tained successively with Powder IV (Foam IV Fig. 4(a) and
238 (b)), Powder V (Foam V Fig. 4(c) and (d)), and Powder VI
239 (Foam VI Fig. 4(e) and (f)). In Foams V and VI, the metal
240 pores clearly replicate in negative the shape of the NaCl
241 particles. With Foam IV, on the other hand, the pores seem
242 somewhat more rounded than the initial powder (compare
243 Fig. 1(IV) and 4(b)). For comparison, the structure of the
244 foam produced from 63 to 90 μm commercial NaCl powders
245 is given in Fig. 4(g) and (h).

246 The NaCl preform made of Powder IV contained around
247 30% porosity. Measuring the volume and the mass of Foam
248 IV yields the expected porosity of 70%. The corresponding
249 values for Powder V and Foam V are respectively, 33 and
250 68%. Aluminium Foam VI on the other hand shows a poros-
251 ity of 53%, while the porosity of the Powder VI NaCl pre-
252 form was 57% and hence differed from the expected value
253 of 47% ($100 - 53$).

254 The internal structure of each foam after compression to
255 the final strain of the test is shown in Fig. 5 by observation
256 of the compression sample surface in the scanning electron
257 microscope after testing (hence the occasional presence of
258 dust particles trapped in the foam). These micrographs are
259 to be compared with those in Fig. 4.

3.3. Mechanical properties of the metallic foams

260
261 Restrictions placed on sample dimensions by the limited
262 batch sizes of “in-house” NaCl powders implied that test
263 specimens were limited to a few millimetres in height. The
264 consequence was that even slight imperfections in the align-
265 ment of parallel faces of the specimens caused significant
266 experimental error in the measured stress–strain curves. This
267 was apparent in that, at low strain, these curves featured an
268 initially low and increasing slope gradually leading to an
269 inflexion point, something that is contrary to the power-law
270 elastoplastic behaviour exhibited at low strain by this class
271 of foam. We provide in Appendix A a simple slice-model
272 analysis of the consequences of non-parallel specimen faces
273 on compression of a power-law material, to show that (i) it
274 explains the observed low-strain stress–strain curve features,
275 and more importantly that (ii) past the point of full contact of
276 the platen with the sample end surfaces, the influence exerted
277 by non-parallel specimen faces on the stress–strain curve

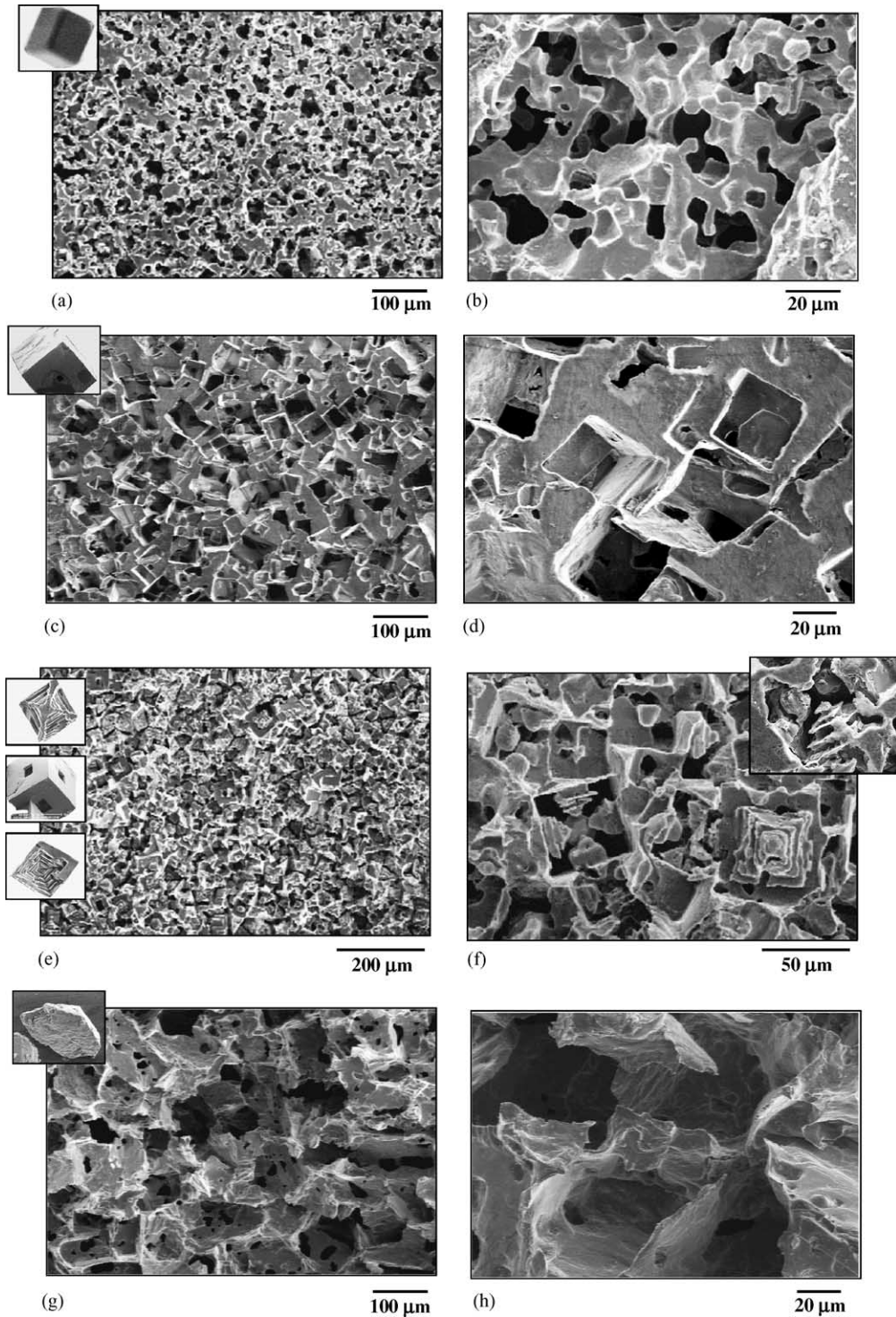


Fig. 4. Aluminium foams obtained (a) and (b) with NaCl Powder IV; (c) and (d) with NaCl Powder V; (e) and (f) with NaCl Powder VI and (g) and (h) with a commercial NaCl powder (on the left side of each micrograph, a reduced micrograph of the NaCl powder morphology is shown).

278 becomes negligible. As a consequence, the only correction
 279 that is required to compensate for this effect is to shift the
 280 strain origin to a proper value. This value is easily deduced
 281 graphically, knowing that the present pure aluminium foam
 282 stress–strain curves obey the standard power law of deformation
 283 with a stress exponent near 0.25 [5]. Lower-strain

284 data are then erased from the curve. The analysis and data
 285 reduction procedure are detailed in Appendix A.

286 All foam compression curves reported here are thus plotted
 287 after correction for non-parallel specimen face artefacts.
 288 Results for Foams IV–VI are given in Fig. 6(a)–(c), respectively,
 289 together with a plot for a foam of similar density

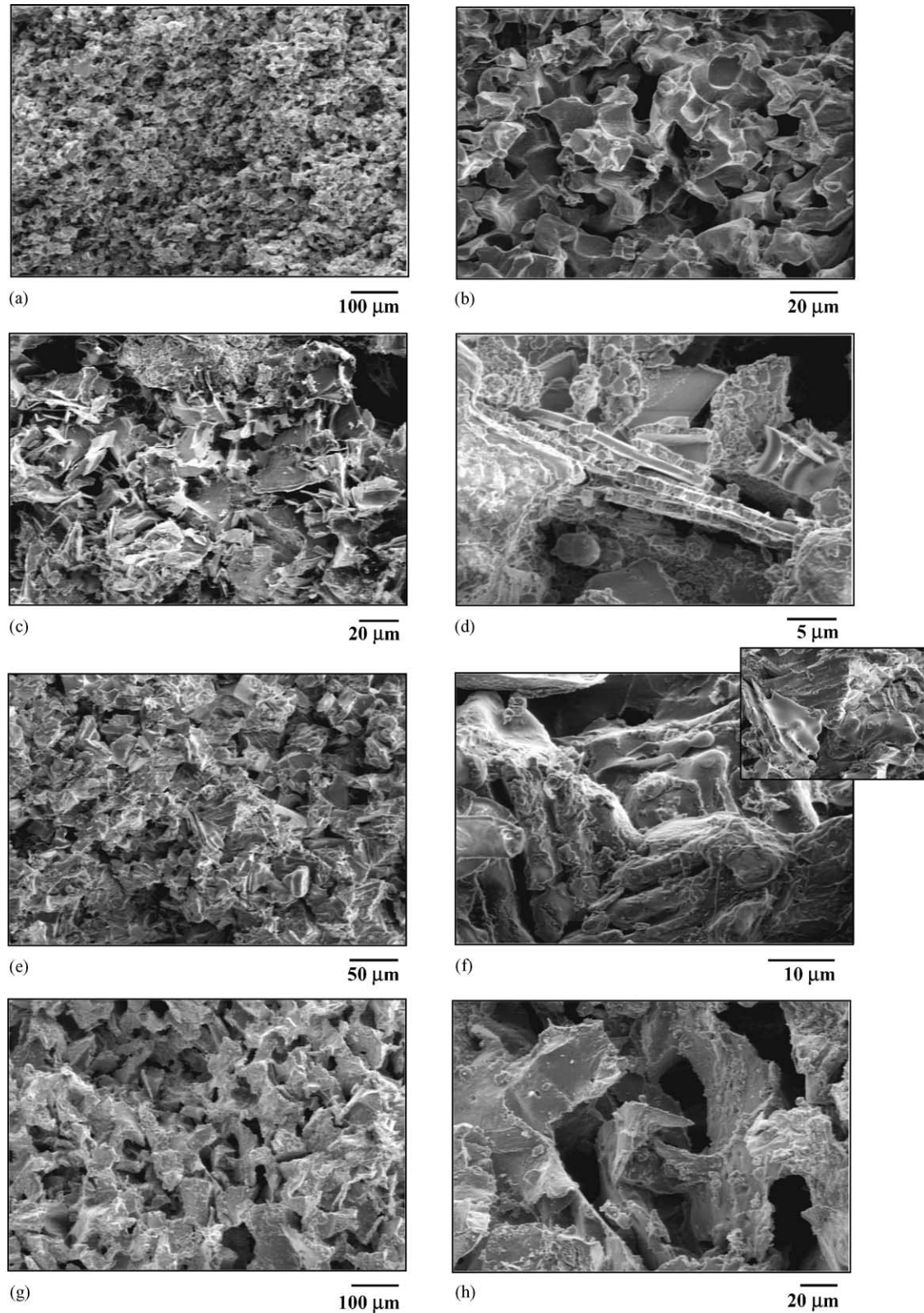


Fig. 5. Aluminium foams after compression (a) and (b) compression of the foam made with NaCl Powder IV; (c) and (d) compression of the foam made with NaCl Powder V; (e) and (f) compression of the foam made with NaCl Powder VI and (g) and (h) compression of a foam made with a commercial 63–90 μm NaCl powder.

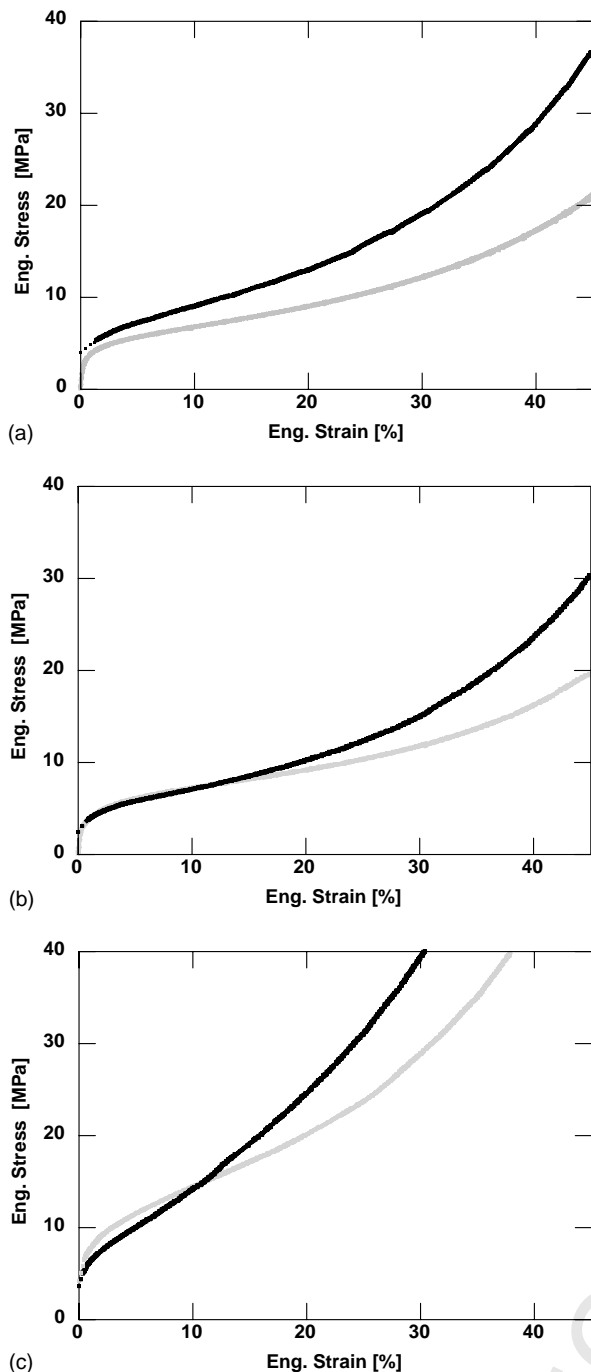


Fig. 6. Engineering stress s –engineering strain e compression curves (a) for Foam IV (—) and a foam made from commercial NaCl particles 10 μm in size of relative density 32% (—); (b) Foam V (—) and a foam made from commercial NaCl particles 63–90 μm in size of relative density 32% (—) and (c) Foam VI (—) and a foam made from commercial NaCl particles 63–90 μm in size of relative density 45% (—). All curves are plotted after data processing as described in Appendix A for correction of non-parallel specimen faces effects.

Fig. 6(b) and (c)), respectively densified to densities near those of Foams IV and V (32 vol.%) and VI (45 vol.%).

4. Discussion

4.1. Factors controlling the NaCl crystallisation

Additives, even in small quantities, clearly influence the precipitation of NaCl from brine with ethanol as the “anti-solvent”. Additives can be selectively adsorbed on crystal facets, such that the growth of individual nuclei is deactivated and the interfacial energy between the crystal and the solution is altered; these changes in turn influence the particle size distribution and the particle morphology [16].

Organic polymers are known to influence the crystallisation of solid particles from a solution, by adsorption at the solid–liquid interface. The particle size or morphology of the precipitating powder can then depend on the molecular weight, concentration, global charge or conformation of polymers [17–19]. This can be explained by steric constraints or structure-directing interactions of the polymers on the nucleation and crystal growth of the inorganic powders [20–23]. Given the low polymer concentration and the large size of polymeric molecules, it is reasonable to expect that the polymer distribution on each facet is not homogeneous: this may be why non-equiaxed particles are obtained.

With sodium hydroxide, two anionic species can be created in solution: hydroxyl anions, and ethanolate anions formed by reaction of hydroxyl anions with the ethanol solvent. These anions may be directly adsorbed onto the growing particle surface and act as growth modifiers, resulting in the observed strong crystal morphology modification. Since the infrared spectrum of Powder II shows no evidence for the adsorption of ethanolate anions, it is most reasonable to conclude that hydroxyl adsorption is responsible for the growth-induced particle shape modification (hydroxyl adsorption cannot be distinguished from water adsorption in the range 3000–3600 cm^{-1}).

With citric acid, Powder III, the stairs descending towards the cube centre from their edges can be explained as resulting from a disturbance in the growth of facets from the edge inwards [24]. The presence of citric acid was identified on the IR spectrum of particles of Powder III Fig. 3(c). This implies effective adsorption of carboxylic acid onto the particles: adsorption of this species must be responsible for the observed stairs. This is not surprising since it has recently been stated that citric acid exerts a strong influence on the growth morphology of calcite [25]. For calcite, it has been found that the organic acid is adsorbed onto the $\{110\}$ crystal faces via the carboxylic acid groups, which produces crystal elongation along a preferential axis. This effect increases with the citric acid concentration.

To explain the differences induced by agitation (Powder VI), one can suppose that (i) particle growth is destabilised

and relatively close pore size produced using commercial NaCl powders. Specifically, the commercial salt was sieved into two size ranges: near 10 μm (comparable to Foam IV Fig. 6(a)) and 63–90 μm (comparable to Foams V and VI

346 by stirring and (ii) growing particles are broken. Attentive
347 examination of recorded micrographs shows indeed that hol-
348 low pyramids can be directly formed by fragmentation of the
349 pierced cube-like particles: the observed hollow pyramids
350 correspond to an interior face of the observed hollow-faced
351 cube-like particles of Powder III.

352 To summarise, one can rationalise some of the differences
353 in the powder morphology by assuming citric acid adsorp-
354 tion on growing NaCl particles with 1 mol/l citric acid, re-
355 sulting in complicated particle shapes. On the other hand,
356 little adsorption seems to occur at an acid concentration of
357 0.06 mol/l: the organic acid seemingly then only acts as a
358 size stabiliser and agglomeration reducer.

359 4.2. The metallic foam structure

360 Comparing Powder IV with Powder V reveals that the
361 use of similar cube-shaped NaCl particles of different sizes
362 leads to different foam morphologies: the smaller cubic par-
363 ticles of Powder IV produce an aluminium foam with smooth
364 and rounded struts (Fig. 4(a) and (b)) while the larger par-
365 ticles of Powder V, also of cubical shape, lead to a foam
366 with far more angular and neatly cubical voids (Fig. 4(c)
367 and (d)). Although the finer Powder IV cubes are indeed a
368 bit more rounded than the larger Powder V cubes, the dif-
369 ference between the two metal foams exceeds that a priori
370 expected given the initial particle shape alone. This differ-
371 ence between the two foams must therefore be attributed to
372 a difference in sintering behaviour during the time spent by
373 the preform in the infiltration furnace (1 h at 710 °C). This
374 makes sense: transport processes responsible for powder sin-
375 tering and pore rounding are known to be far more rapid and
376 potentially different with finer powders, i.e. for Powder IV
377 than for Powder V [26]. We note in passing that Foam IV
378 is perhaps the finest low-density aluminium foam produced
379 to date.

380 The comparatively higher density of Foam VI is explained
381 by the lower initial salt preform density obtained with Pow-
382 der VI. This is not unexpected, given the more intricate and
383 hollow particle shapes obtained. The difference between the
384 observed porosity of Foam VI, of 53%, and the expected
385 porosity based on the density of the Powder VI NaCl pre-
386 form, of 43% (100 – 57), is a sign of incomplete infiltration
387 of the preform by the metal. This is in all likelihood due
388 to closed voids in individual NaCl particles forming Pow-
389 der VI. Given the presence of hollows in the particles, this
390 would indeed be realistic.

391 4.3. Mechanical behaviour

392 Many aluminium foams tested in compression [27–31]
393 exhibit a stress–strain behaviour similar to the idealised
394 schematic curve proposed by Gibson and Ashby [32] for
395 foams made of an elastic–perfectly plastic material, namely
396 (i) stress rising linearly with strain at low stresses (elastic
397 deformation), followed by (ii) a nearly flat portion of the

398 curve called the “collapse plateau” and finally, (iii) a densifi-
399 cation regime where the cell walls come in contact one with
400 another, causing an abrupt rise in the flow stress. Unlike the
401 Gibson–Ashby model (where the plateau is a result of the as-
402 sumed perfectly plastic behaviour), the plateau observed on
403 the compression curves of today’s commercial closed-cell
404 aluminium foams results from localisation of their plastic
405 deformation: cells collapse in successive discrete bands at a
406 relatively constant stress [33–37].

407 The aluminium foams produced here by the replication
408 process behave differently. Setting aside the very early
409 stages of foam deformation, which as shown are influenced
410 by slight imperfections in test specimen face alignment
411 (see Appendix A), two regimes can be distinguished in
412 the present compressive stress–strain curves, consistent
413 with what was found in an earlier investigation of similar
414 replicated pure aluminium foams [5]:

- (i) a region of power-law deformation with a strain expo- 415
nent near 0.25 where the engineering stress s is related 416
to the engineering strain e by: 417

$$s = Ke^{0.25e}; \quad (1) \quad 418$$

- (ii) a region at higher strains where both the stress and the 419
rate of work hardening rise above values corresponding 420
to the power-law behaviour of Region (i). 421

422 No stress plateau is thus observed, furthermore, the foam
423 deforms homogeneously throughout the test, with no visible
424 collapse bands. Values for K in Region (i) of foam deforma-
425 tion for the present foams are reported in Table 2. Accord-
426 ing to San Marchi and Mortensen [5], two work hardening
427 mechanisms operate in the present foams: (i) the intrinsic
428 work hardening inherent to deformation of the metal mak-
429 ing the foam and (ii) another mechanism, which increases
430 in importance as the foam is compressed to become notice-
431 able above a compressive strain on the order of 10%. The
432 power-law behaviour is expected to result from the first work
433 hardening mechanism alone, based on elementary mechan-
434 ical analysis [5]. The second work hardening mechanism is
435 at present not fully identified, however, as argued in ref. [5]
436 available evidence suggests that it involves strut impinge-
437 ment, i.e. the formation of new solid material contacts across
438 the open pores of the foam, to an extent that increases grad-
439 ually with foam compression.

440 To evaluate the strain at which the second mechanism
441 becomes noticeable and to compare the mechanical behav-
442 iour of the various specimens we define the “transition
443 strain” e_t as that where the stress–strain curve deviates from
444 power-law behaviour of Region (i), Eq. (1). This strain was
445 measured at the point where curves of $e^4 = f(e)$ deviate
446 from a straight line (Fig. 7) resulting values for e_t are given
447 in Table 2.

448 Comparing the finest foams, i.e. Foam IV and the com-
449 mercial 10 μm salt foam, it is difficult to reach a conclusion
450 concerning the influence of pore shape on flow stress param-
451 eter K . Indeed, this parameter is significantly higher for the

Table 2
Foam mechanical behaviour parameters

Precursor salt	IV	Commercial	V	Commercial	VI	Commercial
Particle size (μm)	5	10	50	63–90	50	63–90
$V_{f,Al}$ (%)	31	32	32	32	47	45
e_t (%)	6.4	8.9	7.3	10.1	3.1	4.7
K (MPa)	4.8	3.8	3.9	4.0	6.4	7.6

$V_{f,Al}$ is the volume fraction of metal in the foam, e_t the transition strain defined as the strain where the curve $e^4 = f(e)$ deviates from a straight line and K a proportionality constant in the power-law relation ($s = Ke^{0.25}$) describing the beginning of the stress–strain behaviour of replicated Al foams in compression.

452 more regularly structured Foam IV; however, there is also
453 a scale (i.e. pore-size) effect in replicated aluminium foams
454 akin to what is seen in composites: the flow stress of the foam
455 rises with decreasing pore size [38]. For this reason, it can-
456 not be said to what extent the difference in K is a pore scale
457 or pore shape effect. Examination of the data (Fig. 7) sug-
458 gests that the scaling effect is dominant. Indeed, the curves

459 are nearly parallel, which suggests a uniform hardening of
460 the metal, also, there is no such effect with Foam V.

461 Foams V and VI can be compared with commercial salt
462 foams of similar pore size and density (Table 2). Foam
463 VI has a somewhat lower flow stress constant K than its
464 equal-density commercial-salt counterpart. This is not sur-
465 prising given the morphology of Powder VI, with its numer-
466 ous pyramids. These constitute “dead metal” regions that
467 contribute essentially nothing to load bearing in the foam,
468 raising its density with no benefit in terms of foam mech-
469 anical performance at low strain. In other words, at a given
470 volume fraction of metal, the amount of material constitut-
471 ing the struts is lower in Foam VI, lowering in turn the flow
472 stress compared with the foam made with commercial salt.

473 Comparing Foam V and the commercial 63–90 μm salt
474 foam of the same density one finds that K varies on the other
475 hand relatively little, despite the rather different internal
476 architecture of the two pairs of foam (compare respectively
477 Fig. 4(c) and (d) with Fig. 4(g) and (h)). The implication
478 must then be that initial deformation of the foams is pri-
479 marily concentrated in regions that have a relatively similar
480 shape and orientation regardless of the overall pore shape.
481 Most likely, these are narrower metal struts inclined perpen-
482 dicularly to the stress axis. There is, indeed, in both foam
483 types significant bending of narrower struts after deforma-
484 tion (Fig. 5).

485 Taken together, the present data indicate that the influence
486 of pore shape on the flow stress constant at lower strain
487 is relatively minor for the range explored here. The main
488 reason for a decrease in flow stress seems to be the presence
489 of highly convex pore surfaces, which raise the foam density
490 by addition of “dead metal” that does not contribute to load
491 bearing in the foam.

492 The transition strain, e_t , on the other hand, varies sig-
493 nificantly with the foam internal structure (Table 2) (com-
494 pare also the curves in Fig. 6). For all three more regularly
495 shaped and sized “anti-solvent precipitation” salt foams the
496 transition strain is about 25% lower than its value for cor-
497 responding foams made with commercial salt. In the higher
498 strain regime the former thus have a higher flow stress than
499 the latter.

500 For Foam VI this is expected if indeed deviations upwards
501 from the power-law are due to strut impingement: NaCl
502 particle facet hollows result in a foam structure containing

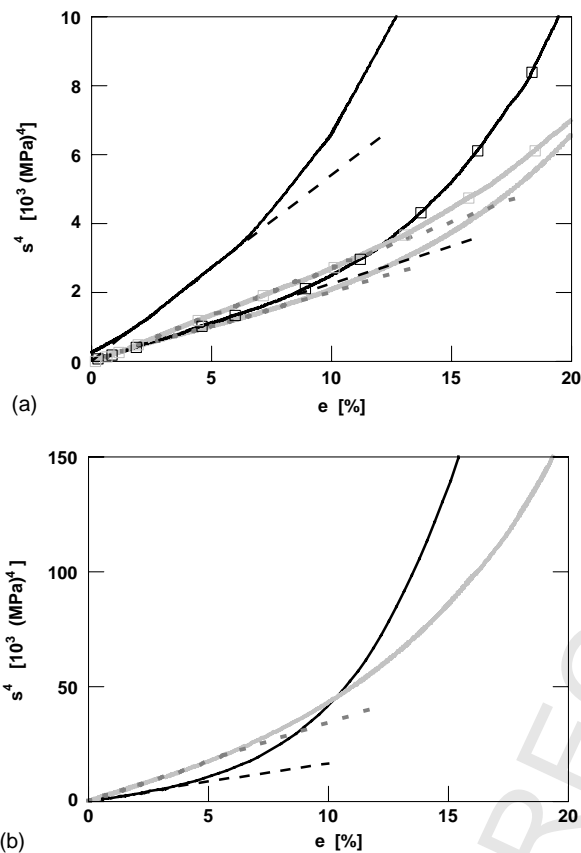


Fig. 7. Engineering stress s raised to the power four as a function of engineering strain e . (a) Foam IV (—), to be compared with commercial 10 μm salt foam (---), and Foam V (⊖) to be compared with commercial 63–90 μm salt foam (⊖). Volume fraction of metal in all foams, $V_{f,Al}$, is close to 32%. Dotted straight lines represent an extrapolation of the power-law strain hardening behaviour $e = s^n$ with $n = 0.25$. (b) Foam VI ($V_{f,Al} = 47\%$) (—), and foam from commercial 63–90 μm salt ($V_{f,Al} = 45\%$) (---). Dotted straight lines represent an extrapolation of the power-law strain hardening behaviour $e = s^n$ with $n = 0.25$.

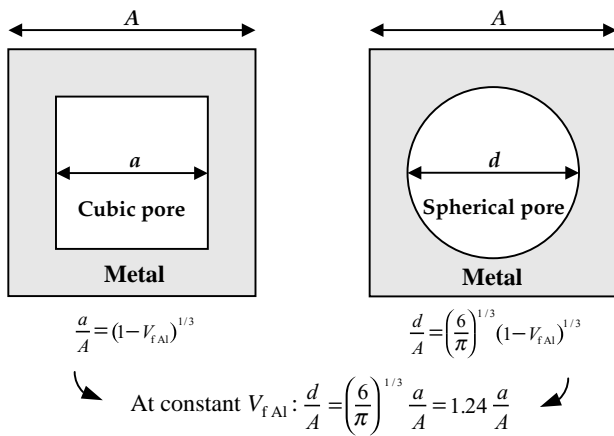


Fig. 8. Schematic illustrating the difference in foam compressive strain when opposite pore sides touch for a cubic and a spherical pore in a foam. A is the size of a representative element of foam volume, a the size of a cubic pore, d the diameter of a spherical pore and V_{fAl} the volume fraction of metal (aluminium) in the foam.

convex pyramids. These are bound to touch at lower strains than concave pores of the foam produced with commercial salt, as seen indeed in Fig. 5(e) and (f).

Foams IV and V also show earlier dominance of the second hardening mechanism attributed to strut impingement than corresponding foams produced from commercial powders. Here, the reason is less obvious, as there are no convex geometrical features in these foams such as the pyramids of Foam VI; however, one can still argue that the cubical pores of this foam are less convex than the nearly spherical pores of the commercial NaCl foams. If we assume for simplicity that strut impingement becomes significant when nearest opposing pore faces begin to meet in regions of high local foam deformation, it follows that the rounder the pores, the later strut contact should set in. This is illustrated in simple terms in Fig. 8: strut contact should appear in a foam with cubical pores (\approx Foams IV and V) at a strain roughly equal to 80% of the strut contact strain for a foam of equal density containing spherical pores (\approx commercial powder foams). This is roughly the difference in transition strain between the two foam types. This explanation thus accounts for the difference observed; however, it is of course very tentative and incomplete. Indeed, local strains for pore face contact are far higher than the observed foam transition strains e_t , the transition strain for Foam VI should then be even lower, and perhaps strut contact is not the reason for the increased rate of work hardening. This interpretation would indicate that, the less convex the pore shape is, the earlier the stress–strain behaviour of a replicated foam should deviate upwards from the power-law behaviour of the metal of which it is composed.

At still higher strains as shown in Fig. 5 that in Foam V flat aluminium facets formed between salt cubes have collapsed, resulting in a structure that resembles a loose piling of aluminium platelets: clearly, local crushing of individual pores has occurred.

5. Conclusion

Five different NaCl particles morphologies have been produced by “anti-solvent” precipitation of NaCl from brine using ethanol in the presence of one of the following additives: poly(acrylic acid), sodium hydroxide or citric acid. With citric acid the additive concentration plays a role in determining the NaCl crystal morphology, as do physical precipitation parameters such as agitation or coarsening time.

The present anti-solvent precipitated NaCl particles can be divided in two categories according to the particle size range. Low concentrations of citric acid or polyacrylic acid lead to fine NaCl particles (smaller than $15\ \mu\text{m}$). Particles with complex morphologies and of average size above $15\ \mu\text{m}$ are obtained with higher concentrations of sodium hydroxide or citric acid additives. With citric acid, additive adsorption is shown to play a role in precipitation.

Replication processing can be used to produce aluminium foams from these particles, with pores down to $5\ \mu\text{m}$ in average diameter. Compressive stress–strain curves display a power-law hardening region, followed by a region of increasing apparent work hardening rate, consistent with an earlier study of replicated aluminium foam. It is found that the particle shape exerts relatively little influence on the low-strain power-law constant. On the other hand, the powder shape influences significantly the strain at which the foam stress–strain curve deviates from power-law behaviour. This deviation is observed with foams produced from regularly shaped and sized cube-derived NaCl particles at a compressive nominal strain around three-quarters its value for less regular and more rounded commercial salt. Assuming that this deviation is caused by mutual strut impingement during deformation, this study indicates that, the less convex the pore shape is, the earlier the deviation in flow stress upwards from power-law behaviour is in replicated aluminium foams.

Acknowledgements

This work was funded by the Swiss National Science Foundation, Project No. 21-58839.99.

Appendix A. Cylindrical metal foam sample compression testing: influence of sample face misalignment

Consider a cylindrical sample of metal foam, of diameter $2r = d$ and height L_0 , that has its top and bottom surfaces slightly non-parallel. It is tested in compression between two parallel platens. If α is the angle between the two non-parallel sample faces, we define the misalignment parameter a as $a = d \tan(\alpha)$ (Fig. 9). Unless the top and bottom sample faces are grossly misaligned, $a \ll L_0$.

586 We assume that, as found in an earlier study [5], the
 587 metal foam material exhibits common power-law (exponent
 588 n) hardening behaviour in engineering stress–strain coordi-
 589 nates, $s = Ke^n$ where s is nominal (engineering) stress,
 590 $e = \Delta L/L_0$ with $\Delta L = L_0 - L$ is the nominal (engineer-
 591 ing) strain and K is a constant. During the compression test,
 592 the force $f(x)$ exerted on a sample slice of thickness dx and
 593 constant height located at distance x from the axis of the
 594 cylinder is:

$$f(x) = 2k \left(\frac{(a/2r)(r-x) - (a - \Delta L)}{L_0} \right)^n \sqrt{r^2 - x^2} dx \quad (A-1)$$

598 when the compression platens have moved closer to one
 599 another by distance ΔL measured from the moment of first
 600 contact with the highest point of the cylinder (Fig. 9)

601 Assuming that the responses of the different slices are in-
 602 dependent from one another (i.e. using a simple slice model),
 603 the global force $F = pr^2s$ on the specimen is:

$$F = \int_{-r}^C \left[2k \left(\frac{(a/2r)(r-x) - (a - \Delta L)}{L_0} \right)^n \sqrt{r^2 - x^2} \right] dx \quad \text{for } L = a \quad (A-2a)$$

608 with $-r \leq x \leq C$ and $C = r((2\Delta L/a) - 1)$, and

$$F = \int_{-r}^r \left[2k \left(\frac{(a/2r)(r-x) - (a - \Delta L)}{L_0} \right)^n \sqrt{r^2 - x^2} \right] dx \quad \text{for } L = a \quad (A-2b)$$

611 Fig. 10 shows, after numerical integration of these equa-
 612 tions, the influence of varying misalignment a on the re-
 613 sulting engineering stress–engineering strain curve from the
 614 compression test, all other parameters remaining constant.

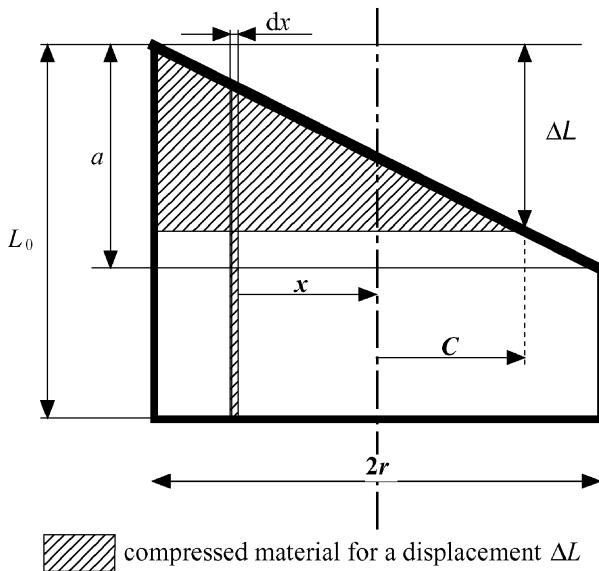


Fig. 9. Profile drawing of compressed cylindrical sample with non-parallel faces, defining parameters in the calculation.

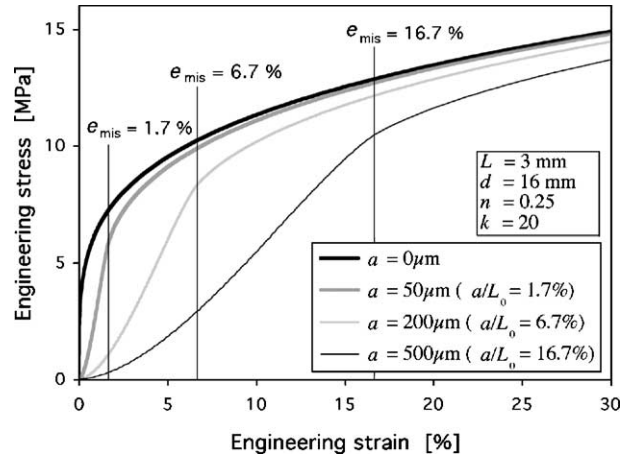


Fig. 10. Calculated apparent stress–strain curves with varying misalignment for a typical sample of aluminium foam; relevant parameters are indicated on the plot.

615 These curves display the general shape of experimental
 616 curves found in the present experiments, indicating that the
 617 initial portion of the curves in this work is indeed influ-
 618 enced by face misalignment (the effects of which become
 619 noticeable because of the small sample height L_0).

620 If we consider a foam of strain hardening exponent $n \approx$
 621 0.25 (as found for replicated pure Al foams produced analo-
 622 gously to the present material [3]), a plot of s^4 versus e will
 623 yield a straight line in the absence of misalignment ($a = 0$).
 624 With $a > 0$, the s^4 versus e curve does not follow a straight
 625 line at small strain; however, as shown in Fig. 11, calcula-
 626 tions show that once the apparent engineering strain $\Delta L/L_0$
 627 exceeds $e_{mis} = a/L_0$, the curve very rapidly becomes linear
 628 and parallel to the s^4 versus e curve obtained with $a = 0$.
 629 Past this point, thus, the engineering stress–strain curve is
 630 essentially unaffected by misalignment. In short, misalign-
 631 ment perturbs the stress–strain curves mainly by causing an
 632 artificial shift in the strain origin. This creates an inflexion

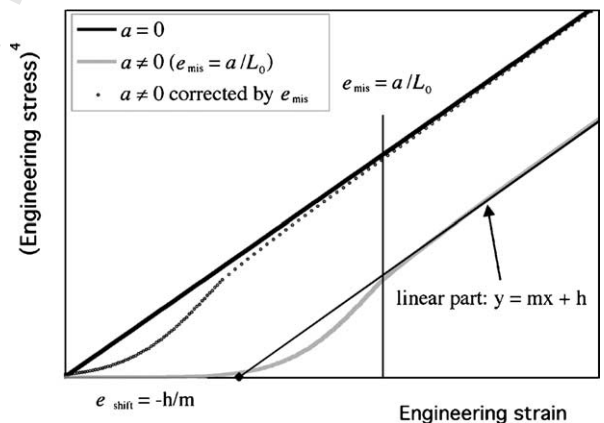


Fig. 11. Same as Fig. 10 in coordinates of s^4 vs. apparent strain $e = \Delta L/L_0$, showing that the plots are essentially identical past the point where $\Delta L = a$, save for an artificial shift in the strain origin caused by the misalignment.

633 point in the curve, before which the data have no real sig-
634 nificance.

635 Compressive engineering stress–strain curves measured
636 in this work were thus plotted with a strain origin defined at
637 the intercept with the horizontal axis of the extrapolated lin-
638 ear curve through s^4 plotted versus $(\Delta L/L_0)$. Such a linear
639 portion was present for all samples tested here, confirming
640 that $n \approx 0.25$ for these pure aluminium foams. The early
641 portions of the data are plotted as a dotted line, to indicate
642 that these portions of the stress–strain curves are to be dis-
643 carded.

644 We note in closing that, were the misalignment caused by
645 lack of parallelism of the platens and not the sample faces,
646 the derivation and the consequences are essentially the same.

647 References

- 648 [1] J. Banhart, Prog. Mater. Sci. 46 (2001) 559. 674
- 649 [2] H.P. Degischer, in: H.P. Degischer, B. Krist (Eds.), Handbook of 675
- 650 Cellular Metals, Production, Processing, Applications, Wiley-VCH, 676
- 651 Weinheim, Germany, 2002, pp. 5–70 (Chapter 2). 677
- 652 [3] C. San Marchi, A. Mortensen, Infiltration and the replication pro- 678
- 653 cess for producing metal sponges, in: H.P. Degischer (Ed.), Hand- 679
- 654 book of Cellular Materials, Wiley-VCH, Weinheim, Germany, 2002, 680
- 655 pp. 43–55. 681
- 656 [4] L. Polonsky, S. Lipson, H. Markus, Modern Cast. 39 (1961) 57. 682
- 657 [5] C. San Marchi, A. Mortensen, Acta Mater. 49 (2001) 3959. 683
- 658 [6] F. Han, H. Cheng, J. Wang, Q. Wang, Scripta Mater. 50 (2004) 684
- 659 13. 685
- 660 [7] T.G. Zijlema, G.J. Witkamp, G.M. Van Rosmalen, J. Chem. Eng. 686
- 661 Data 44 (1999) 1338. 687
- 662 [8] T.G. Zijlema, R.J. Hollman, G.J. Witkamp, G.M. Rosmalen, J. Cryst. 688
- 663 Growth 198–199 (1999) 789. 689
- 664 [9] T.G. Zijlema, G.J. Witkamp, G.M. Van Rosmalen, J. Chem. Eng. 690
- 665 Data 44 (1999) 35. 691
- 666 [10] T. Sata, Ceram. Int. 20 (1994) 39. 692
- 667 [11] S. Al-Jibbouri, J. Ulrich, Cryst. Res. Technol. 36 (2001) 1365. 693
- 668 [12] J.H. Adair, E. Suvaci, Curr. Opin. Colloid Interface Sci. 5 (2000) 694
- 669 160. 695
- 670 [13] M.N. Pons, H. Vivier, T. Rolland, Part. Part. Syst. Char. 15 (1998) 696
- 671 100. 697
- 672 [14] M.N. Pons, H. Vivier, K. Belaroui, B. Bernard-Michel, F. Cordier, 698
- 673 D. Oulhana, J.A. Dodds, Powder Technol. 103 (1999) 44. 699
- [15] R.C. Weast (Ed.), CRC Handbook of Chemistry and Physics, 68th 674
- edition, CRC Press, Boca Raton, Florida, 1987. p. B-130. 675
- [16] J. Nyvlt, J. Ulrich, in: Admixtures in Crystallization, Wiley-VCH, 676
- Weinheim, Germany, 1995. pp. 15–63. 677
- [17] M. Sedlak, M. Antonietti, H. Cölfen, Macromol. Chem. Phys. 199 678
- (1998) 247. 679
- [18] L. Wang, I. Sondi, E. Matijevic, J. Colloid Interface Sci. 218 (1999) 680
545. 681
- [19] V.V. Hardikar, E. Matijevi, Colloids Surf. A: Physicochem. Eng. 682
- Aspects 186 (2001) 23. 683
- [20] E. Dalas, P.G. Klepetsanis, P.G. Koutsoukos, J. Colloid Interface Sci. 684
- 224 (2000) 56. 685
- [21] V. Zaporozhchenko, J. Zekonyte, A. Biswas, F. Faupel, Surf. Sci. 686
- 532–535 (2003) 300. 687
- [22] M. Öner, J. Norwig, W.H. Meyer, G. Wegner, Chem. Mater. 10 688
- (1998) 460. 689
- [23] M.M. Reddy, R. Hoch, J. Colloid Interface Sci. 235 (2001) 365. 690
- [24] J.P. Jolivet, M. Henry, J. Livage, De la solution à l'oxyde - Condensation 691
- des cations en solution aqueuse, Collection Savoirs Actuels, 692
- CNRS Editions, Paris, France, 1994. p. 68. 693
- [25] F.C. Meldrum, S.T. Hyde, J. Cryst. Growth 231 (2001) 544. 694
- [26] W.D. Kingery, H.K. Bowen, D.R. Uhlman, in: Introduction to Ce- 695
- ramics, second ed., Wiley, New York, 1976. pp. 469–515. 696
- [27] T.G. Nieh, K. Higashi, J. Wadsworth, Mater. Sci. Eng. A 283 (2000) 697
- 105–110. 698
- [28] K.C. Chan, L.S. Xie, Scripta Mater. 48 (2003) 1147–1152. 699
- [29] K.Y.G. McCullough, N.A. Fleck, M.F. Ashby, Acta Mater. 47 (1999) 700
- 2323–2330. 701
- [30] E. Andrews, W. Sanders, L.J. Gibson, Mater. Sci. Eng. A270 (1999) 702
- 113–124. 703
- [31] J. Banhart, J. Baumeister, J. Mater. Sci. 33 (1998) 1431–1440. 704
- [32] L.J. Gibson, M.A. Ashby, Cellular Solids: Structure and Properties, 705
- second ed., Cambridge University Press, Cambridge, 1997. 706
- [33] E. Koza, M. Leonowicz, S. Wojciechowski, F. Simancik, Mater. Lett. 707
- 58 (2003) 132–135. 708
- [34] H. Bart-Smith, A.-F. Bastawros, D.R. Mumm, A.G. Evans, D.J. 709
- Sypeck, H.N.G. Wadley, Acta Mater. 46 (1998) 3583–3592. 710
- [35] A.-F. Bastawros, H. Bart-Smith, A.G. Evans, J. Mech. Phys. Sol. 48 711
- (2000) 301–322. 712
- [36] M.F. Ashby, A. Evans, N.A. Fleck, L.J. Gibson, J.W. Hutchinson, 713
- H.N.G. Wadley, Metal Foams: a Design Guide, Boston, MA, But- 714
- terworth Heinemann, 2000. 715
- [37] L.J. Gibson, Annu. Rev. Mater. Sci. 30 (2000) 191. 716
- [38] J.-F. Despois, Y. Conde, C. San Marchi, A. Mortensen, Tensile 717
- behavior of replicated aluminium foams, in: J. Banhart, N.A. Fleck, 718
- A. Mortensen (Eds.), Proceedings of the Conference Metfoam on 719
- Cellular Metals: Manufacture, Properties, Applications, Verlag MIT 720
- Publishing, Berlin, Germany, 23–25 June 2003, pp. 375–380. 721